crystals

MDPI

Article

Porous, Tremella-like $NiFe_2O_4$ with Ultrathin Nanosheets for ppb-Level Toluene Detection

Yanlin Zhang [1], Honglong Qu [1], Cheng Gang [1], Hongtao Guan [1], Chengjun Dong [1,2,*] and Zongyou Yin [2,*]

[1] School of Materials and Energy, Yunnan University, Kunming 650091, China
[2] Research School of Chemistry, Australian National University, Canberra 2601, Australia
* Correspondence: dongcj@ynu.edu.cn (C.D.); zongyou.yin@anu.edu.au (Z.Y.)

Abstract: As a typical spinel ferrite, $NiFe_2O_4$ is suitable for use in gas sensors. Herein, we report the fabrication of porous, tremella-like $NiFe_2O_4$ assembled using porous, ultrathin nanosheets via the coordination of Ni^{2+} and Fe^{2+} with 1,4-phenylenediboronic acid. The optical band gap of the $NiFe_2O_4$ is estimated to be about 1.7 eV. Furthermore, the $NiFe_2O_4$ sensor annealed at 400 °C exhibits a low detection limit of 50 ppb, a fast response/recovery time (11.6 s/41.9 s to 10 ppm toluene), good reproducibility, and long-term stability at 220 °C. The suitable sensing performances can be attributed to the good catalytic activity of $NiFe_2O_4$ to toluene oxidation. Moreover, the ultrathin nanosheets with porous structures provide a large number of active sites to significantly favor the diffusion and adsorption/desorption of toluene molecules. This current work provides an insight into fabricating $NiFe_2O_4$ using 1,4-phenylenediboronic acid, which is promising for ppb-level toluene detection.

Keywords: porous; $NiFe_2O_4$; nanosheet; toluene; gas sensor

Citation: Zhang, Y.; Qu, H.; Gang, C.; Guan, H.; Dong, C.; Yin, Z. Porous, Tremella-like $NiFe_2O_4$ with Ultrathin Nanosheets for ppb-Level Toluene Detection. *Crystals* **2023**, *13*, 865. https://doi.org/10.3390/cryst13060865

Academic Editor: Nabeen K Shrestha

Received: 6 May 2023
Revised: 21 May 2023
Accepted: 23 May 2023
Published: 25 May 2023

1. Introduction

Toluene (C_7H_8) is a typical volatile organic compound (VOC) which is extensively used in medicine, leather, pesticides, laboratory solvents, pharmaceuticals, and so on [1–3]. However, toluene is harmful for both human health and the environment. Exposure to toluene could pose a risk to human health by damaging the central nervous system, liver, kidneys, heart, etc. [4–6]. It is reported that short-term exposure to 70 ppb of toluene may negatively affect the cognitive function of the brain [7]. Furthermore, toluene is reported to be a vital biomarker in the diagnosis of lung cancer. The concentrations of toluene in patients with lung cancer were reported to range from 80 to 100 ppb [8,9]. Hence, rapid toluene detection with excellent selectivity at an early stage is very promising for multiple applications in health care, environmental protection, and medical diagnoses. Among various techniques, resistive gas sensors fabricated with semiconductor metal oxides have attracted wide attention due to their advantages of easy fabrication and low cost [10,11]. However, it is still challenging to improve their sensing performance, especially for selective and sensitive ppb-level toluene detection.

Recently, spinel ferrite materials (AB_2O_4) have shown significant advantages in the detection of various gases due to their unique chemical compositions and crystal structures in which two cation sites are occupied by either transition or post-transition cations [12,13]. The combination of various transition and post-transition metal cations in spinel ferrites could be favorable for a highly sensitive and selective gas sensor. Thus far, sensitive materials such as $NiFe_2O_4$, $ZnFe_2O_4$, $ZnCo_2O_4$, $NiCo_2O_4$, and $NiMn_2O_4$ have been developed for gas sensors [14–16]. $NiFe_2O_4$ is one of the particularly important spinel ferrite materials which has recently been used in a gas sensor for the detection of toluene. Various synthesis methods have been developed to tune the morphology of $NiFe_2O_4$ to improve its sensing properties. For example, Lai et al. used KIT-6 as a template to successfully obtain mesoporous $NiFe_2O_4$, which exhibited an excellent toluene-sensing property [17].

Kim's group synthesized 3D hierarchical $NiFe_2O_4$ porous microspheres with the assistance of urea and glucose. The $NiFe_2O_4$ sensor achieved a good toluene gas response at a low working temperature [18].Yang and his co-workers prepared $NiFe_2O_4$ nanomaterials using a co-precipitation method; these materials exhibited good sensing properties in their sensitivity and selectivity to toluene detection [19]. Paula et al. prepared $NiFe_2O_4$ nanoparticles via levitation-jet synthesis which were shown to be remarkably sensitive to toluene gas. In our previous work, Ni/Fe-MOF-derived 1D porous $NiFe_2O_4$ nanorods showed outstanding selectivity and sensitivity to toluene [20]. Even so, $NiFe_2O_4$-based gas sensors usually exhibit unsatisfied sensing properties in their low gas responses and high detection limits. Therefore, a novel synthesis method is highly desirable for fabricating $NiFe_2O_4$ with a unique microstructure to enhance its toluene detection to the ppb level. Recently, using an organic acid as both a coordinating reagent and a soft template has been an effective way of fabricating metal oxides [21,22]. Studies have shown that boric acid is capable of coupling with the metal ions of Pb^{2+}, Cd^{2+}, and Fe^{2+} to form nanosheet complexes [23–25]. Carboxylphenyl boronic acid was reported to complex with metal ions (such as Zn^{2+}, Cd^{2+}, Ni^{2+}, abd Ln^{3+}) to form 2D coordination polymer nanosheets [26,27]. These pioneered works provide us a clue for synthesizing $NiFe_2O_4$ nanosheets by taking 1,4-phenylenediboronic acid to coordinate with both Ni^{2+} and Fe^{2+} ions.

Herein, we successfully prepared porous, tremella-like $NiFe_2O_4$ with ultrathin nanosheets by using 1,4-phenylenediboronic acid to coordinate Fe^{2+} and Ni^{2+}. Our prepared $NiFe_2O_4$ possesses good crystallinity, catalytic activity, a porous, ultra-thin nanosheet structure, and a large specific surface area (77.8 m^2/g). The sensor based on $NiFe_2O_4$ annealed at 400 °C exhibits good toluene-gas-sensing properties, especially with a low detection limit of 50 ppb. The findings of this study demonstrate the possibility of using 1,4-phenylenediboronic acid to fabricate $NiFe_2O_4$ nanosheets which are then suitable for application in trace toluene detection.

2. Experimental Section

2.1. Fabrication of $NiFe_2O_4$

All the starting reagents were of analytical grade. Deionized water (18 MΩ cm at room temperature) was used for this work. The tremella-like $NiFe_2O_4$ was synthesized via a hydrothermal process followed a thermal treatment. Specifically, 0.5 mmol (0.1188 g) $NiCl_2{\cdot}6H_2O$ (AR 99.9%) and 1 mmol (0.1988 g) $FeCl_2{\cdot}4H_2O$ (AR 98%) were completely dissolved into the mixture of 50 mL N,N-dimethylformamide (DMF) (AR 99.5%) with 5 mL anhydrous ethanol and 5 mL deionized water. Then, 3 mmol (0.4973 g) of 1,4-phenylenediboronic acid ($C_6H_8B_2O_4$) (AR 95%) was further added under magnetic stirring for 30 min to form a homogenous solution. After a hydrothermal reaction at 130 °C for 12 h, the obtained product was separated via centrifugation and rinsed with deionized water and ethanol. Next, the precursor products were collected after being dried at 60 °C for 6 h. Finally, the precursor was annealed in air at 350 °C, 400 °C, and 450 °C for 2 h with a heating rate of 3 °C/min, and the corresponding $NiFe_2O_4$ samples were labeled S-350, S-400, and S-450, respectively.

2.2. Characterization

The crystal phase of the $NiFe_2O_4$ was analyzed on a Rigaku TTRIII X-ray diffraction (XRD) equipped with Cu K_α radiation (1.54056 Å) from a scanning angle of 10° to a scanning angle of 70°. A field emission scanning electron microscope (FESEM, FEI QUANTA 200, Hillsboro, OR, USA) was utilized to analyze the morphological features of all samples. Transmission electron microscopy (TEM) images were taken on JEOL JEM-2100 microscope at an accelerating voltage of 100 kV. The corresponding elemental mapping image was acquired by the EDS attachment on the FESEM. A thermogravimetric analysis (TGA-DSC) was performed to investigate the decomposition of the precursor at a heating rate of 10 °C/min (TA SDT-2960, New Castle, DE, USA). X-ray photoelectron spectra (XPS) were characterized to measure elemental valence states, and the electron binding energy was

calibrated by referring to the C1s peak at 284.6 eV. The UV–visible absorption spectra were tested on a UV–VIS spectrophotometer (SolidSpec-3700). The Brunauer–Emmett–Teller (BET) surface area was derived from nitrogen isotherms measured on a surface adsorption instrument (ASAP 2020 Plus).

2.3. Sensor Fabrication and Testing Properties

The gas sensor was fabricated and tested using our general procedure [28,29]. The as-synthesized $NiFe_2O_4$ powders were dispersed into a certain amount of deionized water and sonicated into a floating solution. The above suspension solution was then coated onto the outer surface of the alumina tube and dried at 120 °C for 2 h. A pair of Au electrodes and corresponding Pt wires at both ends of the alumina tube were set. To ensure good contact between the gold electrode and the sensing material, the sensors were annealed in air at 300 °C for 2 h. The gas-sensing performances were tested using a WS-30 A system (Weisheng Instruments Co., Zhengzhou, China) with a volume of the closed chamber of 18 L. The desired gas concentration was obtained based on the static liquified gas distribution method [28]. The response (β) of the sensor is defined as:

$$\beta = R_g/R_a \quad (1)$$

where R_g and R_a stand for the resistance of the sensor in the target gas and air, respectively. In addition, the response and recovery time were described as the time taken for 90% of the entire resistance change to be achieved. During the test of the gas-sensing properties, the relative humidity (RH) was maintained around 30%.

3. Results and Discussion

The crystalline structures were examined via X-ray diffraction (XRD). The XRD curves of the $NiFe_2O_4$ samples are shown in Figure 1. In comparison with the standard card (JCPDS: 54-0964), a cubic $NiFe_2O_4$ structure (space-group: $Fd\bar{3}m$) can be confirmed. Specifically, the distinct peaks are detected at 2θ of 30.3°, 35.7°, 37.3°, 43.3°, 57.3°, and 63°, corresponding to the Bragg planes of (220), (311), (222), (400), (511), and (440), respectively. The crystallite size of the $NiFe_2O_4$ is estimated by using Scherrer's equation (Equation (2)):

$$D = k\frac{\lambda}{\beta \cos \theta} \quad (2)$$

where D, k, λ, β, and θ are the crystallite size, the Scherrer constant (0.89), the X-ray wavelength (1.54056 Å), the peak width at half, and Bragg's diffraction angle, respectively. It can be calculated that the grain sizes of the S-400 $NiFe_2O_4$ and S-450 $NiFe_2O_4$ are 13.1 and 16.2 nm. Due to the poor crystallinity of the S-350, its grain size cannot be calculated. The X-ray diffraction peak of the materials has no peaks for other impurities, indicating that the $NiFe_2O_4$ is of a high quality. In Figure 1, the XRD peak becomes sharp as the annealing temperature increases, indicating strong crystallinity. The band gap is an important parameter for a metal oxide semiconductor. Therefore, the UV-vis absorption spectra of $NiFe_2O_4$ materials have been studied (Figure 2), and they are used to calculate the band gap using the following equation [29,30]:

$$(\alpha h\nu)^2 = A(h\nu - E_g) \quad (3)$$

where α, h, ν, E_g, and A represent the absorption coefficient, Planck's constant, light frequency, band gap energy, and a constant, respectively. The Tauc-plot of $(\alpha h\nu)^2$ versus the photo energy ($h\nu$) of the $NiFe_2O_4$ (S-350, S-400, and S-450) is as shown in Figure 2b–d. In general, the intercept between the linear portion of the $(\alpha h\nu)^2$ to $h\nu$ plots on the $h\nu$ axis represents the value of the band gap energy (E_g). From Figure 2b–d, it can be seen that the band gap is estimated to be 1.73 eV, 1.70 eV, and 1.72 eV for the S-350, S-400, and S-450 samples. Although the band gap depends strongly on the defect level and

microstructure derived from the different synthetic methods, our values are comparable with some reported values of the ban gaps for pure $NiFe_2O_4$, as summarized in Table 1.

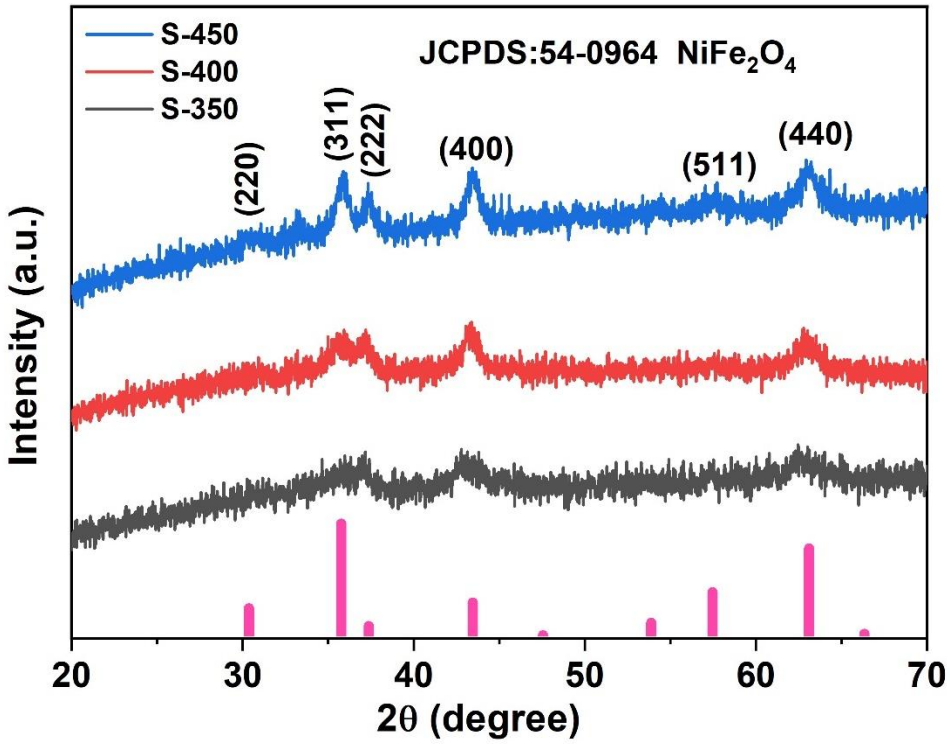

Figure 1. XRD parttern of $NiFe_2O_4$ annealed at 350 °C, 400 °C, and 450 °C with JCPDS No.54-0964.

Table 1. Comparision of band gaps of $NiFe_2O_4$ synthesized with different methods.

Materials	Synthesis Method	Morphology	Annealing (°C)	Band Gap (eV)	Ref.
$NiFe_2O_4$	Co-precipitation	Nanoparticles	700 800 900	1.59 1.67 1.71	[31]
$NiFe_{1.95}Y_{0.05}O_4$			800	1.62	
$NiFe_{1.9}Y_{0.1}O_4$				1.59	
$NiFe_{1.85}Y_{0.15}O_4$				1.59	
$NiFe_{1.8}Y_{0.2}O_4$				1.57	
$NiFe_2O_4$	Co-sputtering ($Ar:O_2$ = 40:60)	Nanoparticles		1.785	[32]
	Co-sputtering ($Ar:O_2$ = 30:70)			1.78	
	Co-sputtering ($Ar:O_2$ = 20:80)			1.779	
$NiFe_2O_4$	Magnetron sputtering	Thin films		1.78	[33]
			400	1.88	
			500	2.46	
			700	2.72	
$NiFe_2O_4$	Co-precipitation	Nanoparticles	700	1.59	[34]
$NiFe_2O_4$	CVD	Thin films		2.34 /2.78	[35]
$NiFe_2O_4$	PLD	Thin Films	690	2.36	[36]
$NiFe_2O_4$	Hydrothermal synthesis	Nano-sheets	350	1.73	This work
			400	1.70	
			450	1.72	

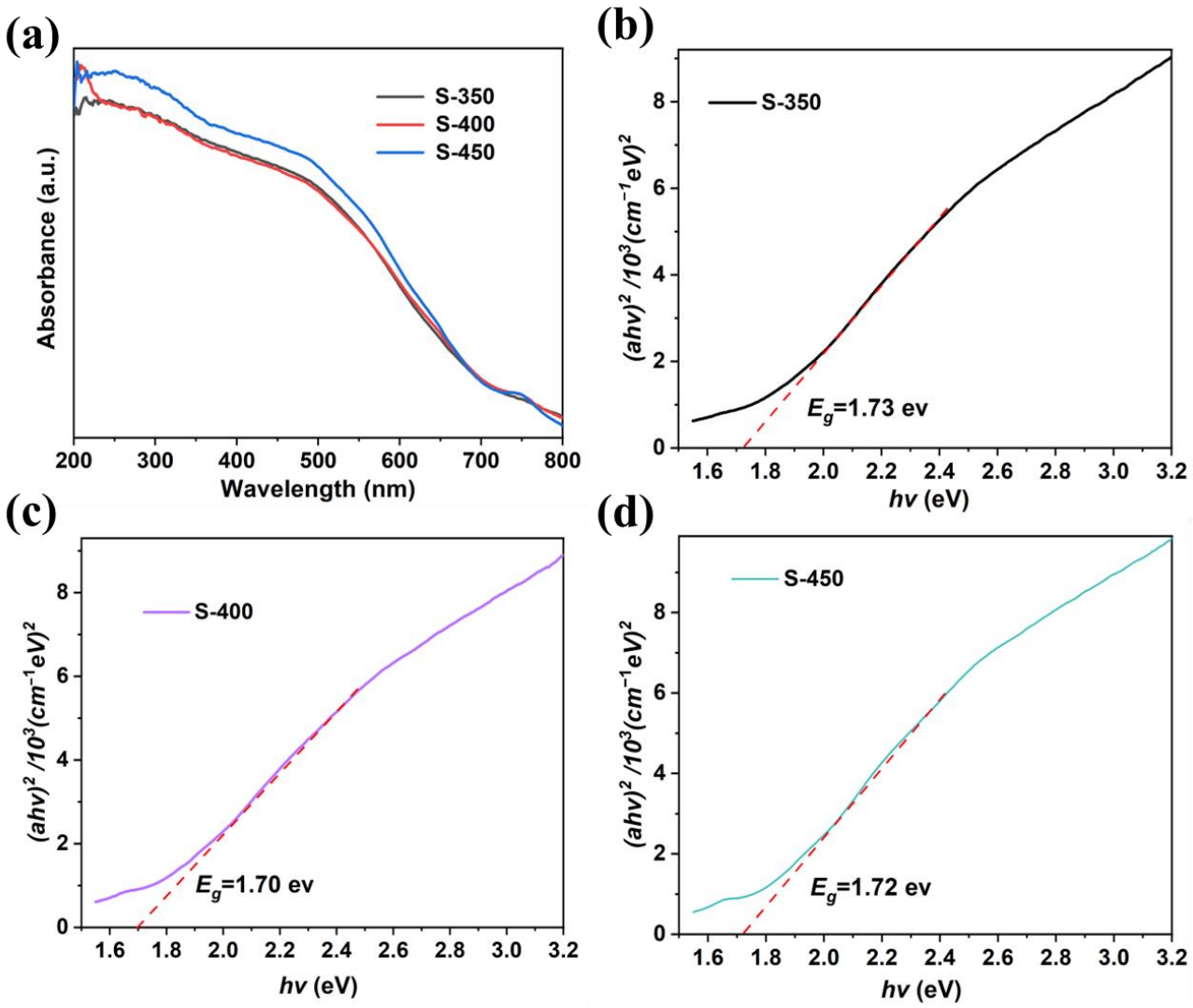

Figure 2. (**a**) UV–vis spectrum absorption spectra and band gap estimations of the tremella-like $NiFe_2O_4$ nanosheets for (**b**) S-350, (**c**) S-400, and (**d**) S-450.

The morphology and microstructure of the $NiFe_2O_4$ were observed via SEM. As can be seen from Figure 3a,b, the $NiFe_2O_4$ precursor shows a nanosheet structure. After being annealed in air, the nanosheets became wrinkled into a tremella-like structure. Similar morphologies are observed after annealing at different temperature of 350 °C (Figure 3c,d), 400 °C (Figure 3e,f), and 450 °C (Figure 3g,h). The $NiFe_2O_4$ exhibits a tremella-like shape with a diameter of 3–4 μm (Figure 3e). In the highly magnified SEM image in Figure 3f, the $NiFe_2O_4$ consists of closely interlaced ultrathin nanosheets, resulting in a porous nanostructure.

The TEM characterization provides more details about the microstructures. It can be seen that the tremella-like S-400 $NiFe_2O_4$ is composed of subunits of ultrathin nanosheets (Figure 4a,b). The ultrathin nanosheet structure is the result of the complex formation of boric acid ligands with Fe^{2+} and Ni^{2+} [37]. The homogeneous distributions of the Ni, Fe, and O elements on the tremella-like $NiFe_2O_4$ are illustrated in Figure 4c. Interestingly, a large number of holes can be clearly observed from Figure 4d. These pores range in diameter from 5 nm to 40 nm. Some typical $NiFe_2O_4$ nanoparticles are from 9.7 nm to 14.2 nm in diameter, as shown in Figure 4e. The HRTEM image (Figure 4f reveals a lattice spacing of 0.25 nm, which is ascribed to the (311) plane of $NiFe_2O_4$, and the results are well matched with XRD analysis.

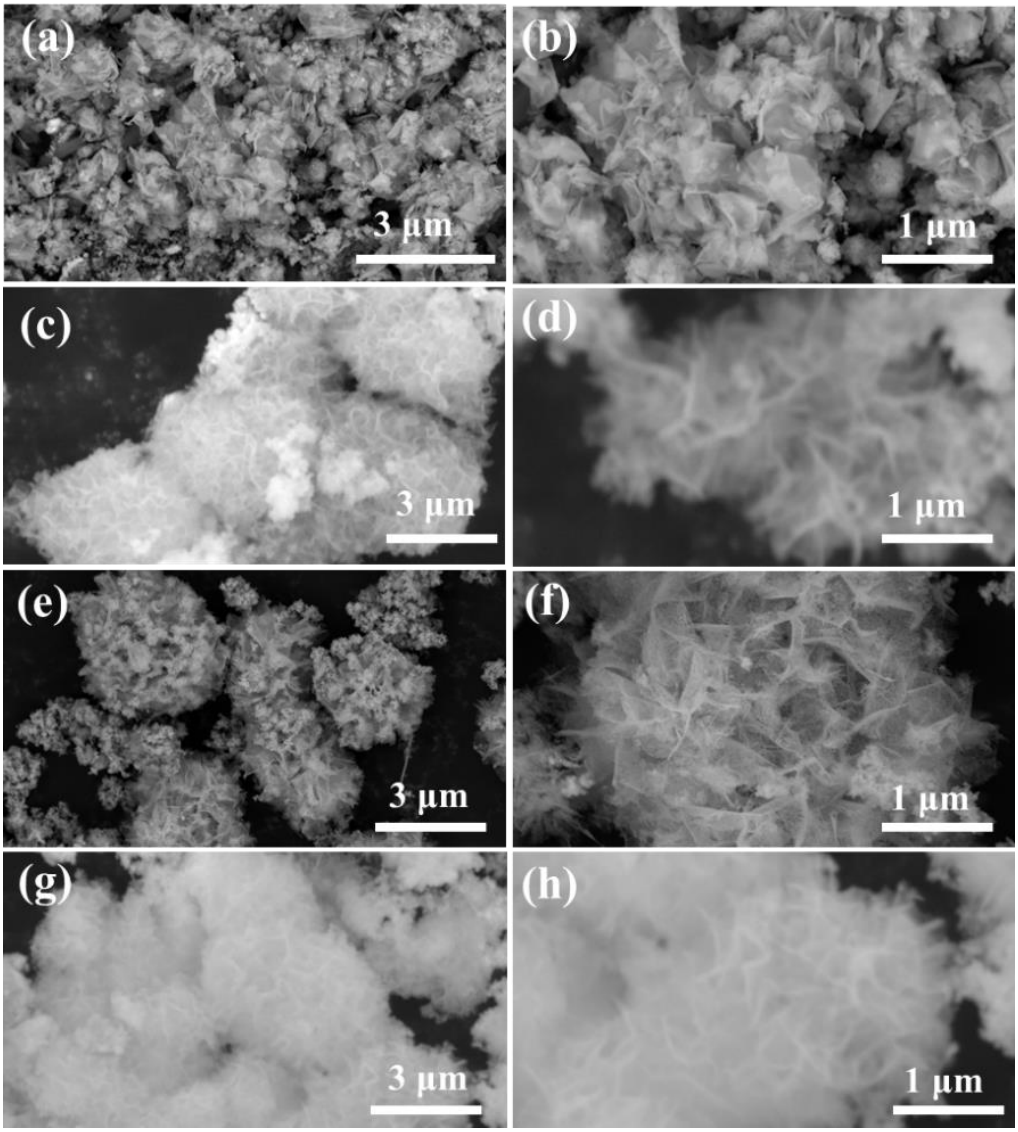

Figure 3. SEM image of (**a**,**b**) precursor, and tremella-like $NiFe_2O_4$ annealed at (**c**,**d**) 350 °C (S-350), (**e**,**f**) 400 °C (S-400), and (**g**,**h**) 450 °C (S-450) in air.

Taking the $NiFe_2O_4$ annealed at 400 °C as an example (S-400), the textural properties of the tremella-like $NiFe_2O_4$ nanosheets were further studied via a nitrogen adsorption–desorption test, as shown in Figure 5. Obviously, the $NiFe_2O_4$ adsorption isotherm belongs to type IV, according to the IUPAC classification [38]. Moreover, the material has an H3-type hysteresis loop, which may be due to the accumulation of several nanosheets forming mesoporous properties. As a result, the unique $NiFe_2O_4$ possesses a high specific surface area of 77.80 m^2/g through the N_2 adsorption–desorption measurement. In addition, the pore distribution can be estimated by the Barrett–Joyner–Halenda (BJH) method, which shows that the average pore size of the $NiFe_2O_4$ is centered at about 18.5 nm (inset in Figure 5). The TEM images in Figure 4d,e reveal that the $NiFe_2O_4$ comprises numerous nanoparticles, giving rise to the formation of pores. The specific area of the $NiFe_2O_4$ is strongly dependent on the synthesis methods and morphologies, as shown in Table 2. Notably, our synthesized tremella-like $NiFe_2O_4$ with nanosheets exhibits a larger specific surface area than common 0D (nanoparticles), 1D (nanofibers and fusiformis), and 3D (nanocubes, hexagonal bipyramids, nanospheres and microspheres) $NiFe_2O_4$ materials. Thus, we provide a facile hydrothermal method using 1,4-phenylenediboronic acid to fabricate porous $NiFe_2O_4$ with high specific surface area which will facilitate the molecules

adsorption and desorption of gas molecules as well as oxidation on the surface, leading to an good gas-sensing performance [39]. Therefore, $NiFe_2O_4$ is expected to show good gas-sensing properties towards toluene detection.

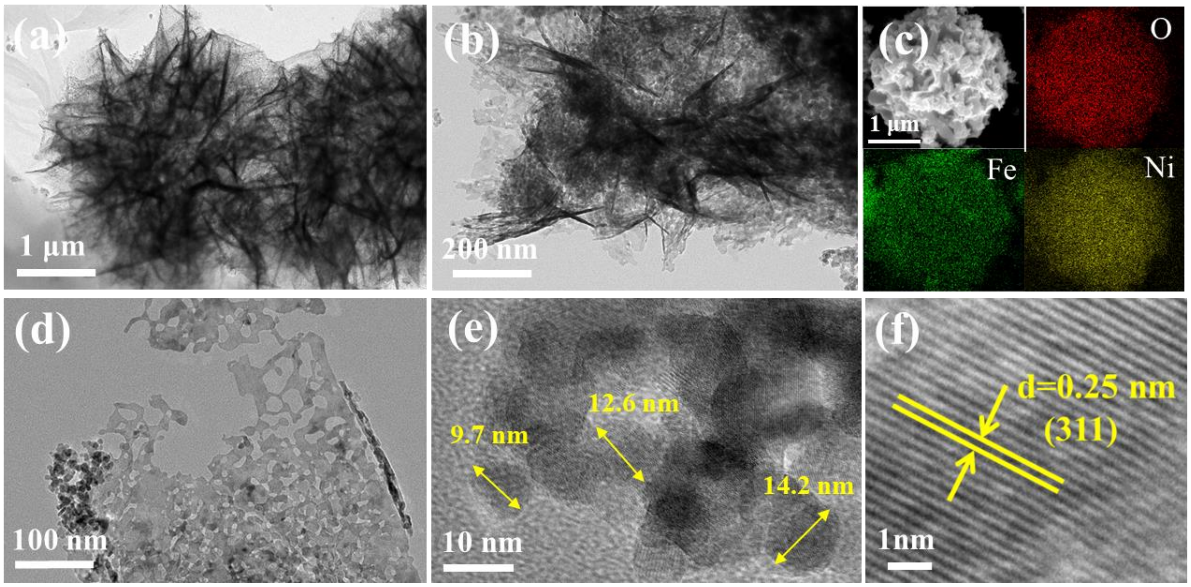

Figure 4. (**a**,**b**) TEM images of tremella-like S-400 $NiFe_2O_4$ nanosheets, (**c**) the EDS mapping of S-400 $NiFe_2O_4$, (**d**,**e**) high-magnification TEM, and (**f**) the HRTEM of S-400 nanosheets.

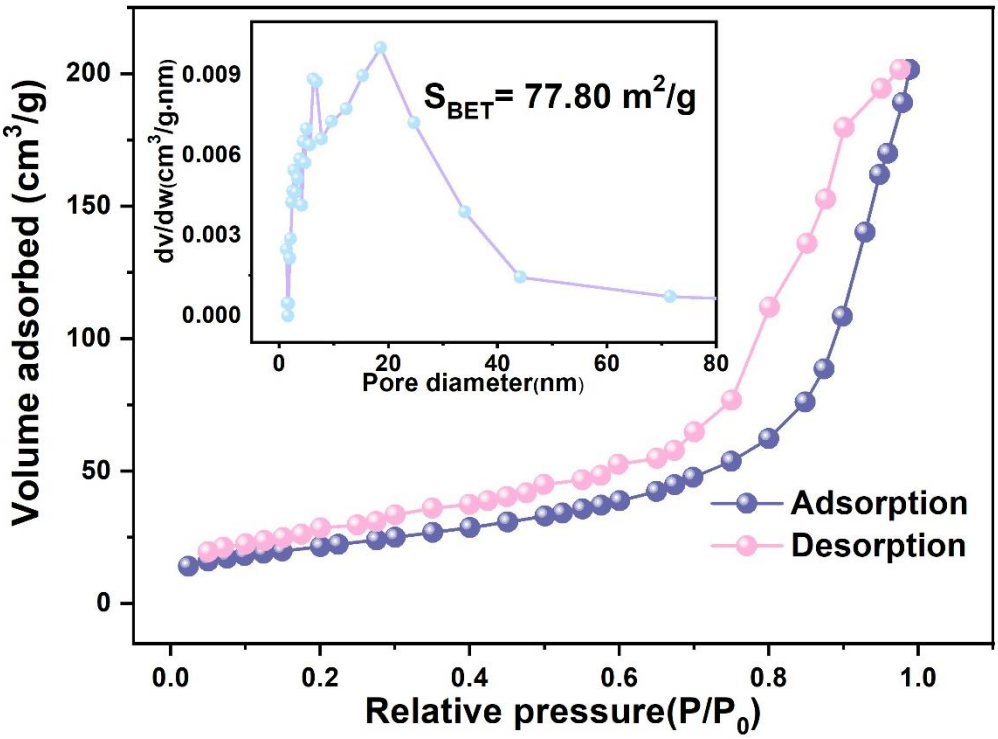

Figure 5. Nitrogen adsorption–desorption isotherms and pore size distributions (inset) of tremella-like $NiFe_2O_4$ (S-400) nanosheets.

Table 2. Comparision of specific surface areas and crystal sizes of $NiFe_2O_4$ synthesized with different synthesis methods and morphologies.

Materials	Synthesis Method	Morphology	Surface Area(m^2/g)	Crystal Size (nm)	Ref.
$NiFe_2O_4$	MOFs templates	Nanocubes	33.72		[40]
$NiFe_2O_4$	MOFs templates	Hexagonal biyramids	64.78		[41]
$NiFe_2O_4$	MOFs templates	Fusiformis	61.50		[42]
$NiFe_2O_4$	Carbon sphere templates	Nanospheres	86.9	16	[43]
$NiFe_2O_4$	Ultrasound assistance	Nanoparticles	17.178	17	[44]
$NiFe_2O_4$	Co-precipitation	Nanoparticles	5.32		[45]
$NiFe_2O_4$	Electrospinning	Nanofibers	54	20	[46]
$NiFe_2O_4$	Hydrothermal	Microspheres	46.44	46.4	[18]
$NiFe_2O_4$	Hydrothermal	Nanosheet	77.80	13.1	This work

1,4-phenylenediboronic acid is rich in carboxyl groups which will easily coordinate with the metal ions of Fe^{2+} and Ni^{2+} to form complexes [47]. In addition, 1,4-phenylenediboronic acid may serve as a capping agent or template for the formation of a nanosheet structure during the synthesis process. In an atmosphere in which DMF is used as a complex solvent, the borate anions in 1,4 p-phenylboronic acid are drawn together with Fe^{2+} and Ni^{2+} via electrostatic interaction and form complexes of specific two-dimensional structures [48]. With subsequent heat treatment, the pyrolysis process occurs in the complex. The $NiFe_2O_4$ was then synthesized after thermal treatment, which was studied via a thermogravimetric analysis (TGA), as shown in Figure 6. It can be seen that the weight loss of the sample is aroud 3.5% below 150 °C, which may originate from the loss of absorbed water in the precursor. As the temperature rises further to 350 °C, the decomposition of the precursor results in a weight loss of approximately 18.4%. The weight loss at this stage is ascribed to the thermal decomposition of the complexes formed from Ni^{2+}, Fe^{2+} and 1,4-phenylenediboronic acid. There is an endothermic peak at a temperature of 257.08 °C, which may be the peak for the decomposition of organic matter to absorb energy. The decomposition of organic matter will release a large amount of carbon dioxide and nitrogen oxide gases [49]. The kinetics of this process are very intense, resulting in a large number of holes in most of the product. After that, a slight weight loss could orignate from the removal of the residual carbon and the further crystallization of the $NiFe_2O_4$.

To identify the elemental compositions and chemical bonding states, the $NiFe_2O_4$ nanosheets were subjected to an XPS analysis. As shown in Figure 7a, the coexistence of Ni, Fe, and O elements on the S-400 $NiFe_2O_4$ was confirmed. The Ni 2p spectrum of the S-400 $NiFe_2O_4$ (Figure 7b) exhibits two spin-orbit doublets characteristic of Ni $2p_{3/2}$ and Ni $2p_{1/2}$ located at 854.11 eV and 873.36 eV, respectively, as well as satellite peaks centered at 861.15 eV and 878.90 eV, corresponding to the characteristic of Ni^{2+} [50,51]. Meanwhile, the Ni $2p_{3/2}$ and Ni $2p_{1/2}$ peaks can be deconvoluted into two peaks at 856.06 eV and 872.69 eV, which are attributed to Ni^{3+} species. Similarly, in the Fe 2p spectrum of the S-400 $NiFe_2O_4$ (Figure 7c), peaks at 713.85 eV and 726.10 eV can be assigned to Fe^{3+}. The binding energies of 710.53 eV and 723.40 eV correspond to Fe^{2+}. The coexistence of Ni^{2+}/Ni^{3+} and Fe^{2+}/Fe^{3+} cations is essential for catalyzing toluene to enhance the sensor's gas-sensing performance [52]. In particular, the formation of high-oxidation states of Ni^{3+} and Fe^{3+} could favor the transport of electrons and the formation of abundant oxygen ions to catalyze the reaction of the target gas molecules for a high degree of sensitivity [53]. The O 1s peak in XPS (Figure 7d–f) is asymmetric in shape and can be divided into two major peaks. Taking the S-400 sample as an example (Figure 7e), the low binding energy of 530.06 eV at the peak is characteristic of lattice oxygen ($O_{lattice}$), which does not react with the target gas. Conversely, at relatively high binding energies (532.00 eV), a well-resolved peak is assigned to surface-adsorbed oxygen, which is thought to react with the target gas molecules to determine the gas-sensing characteristics [54]. Although a similar behavior of O 1s was

observed, the ratios of adsorbed oxygen were estimated to be 13.12%, 23.79%, and 20.16% for S-350, S-400, and S-450 $NiFe_2O_4$ (Figure 7d–f), respectively. These results indicate that the S-400 $NiFe_2O_4$ could show a better sensing property because the adsorbed oxygen will evolve into active oxygen species to enhance the reaction with the target gas molecules [8].

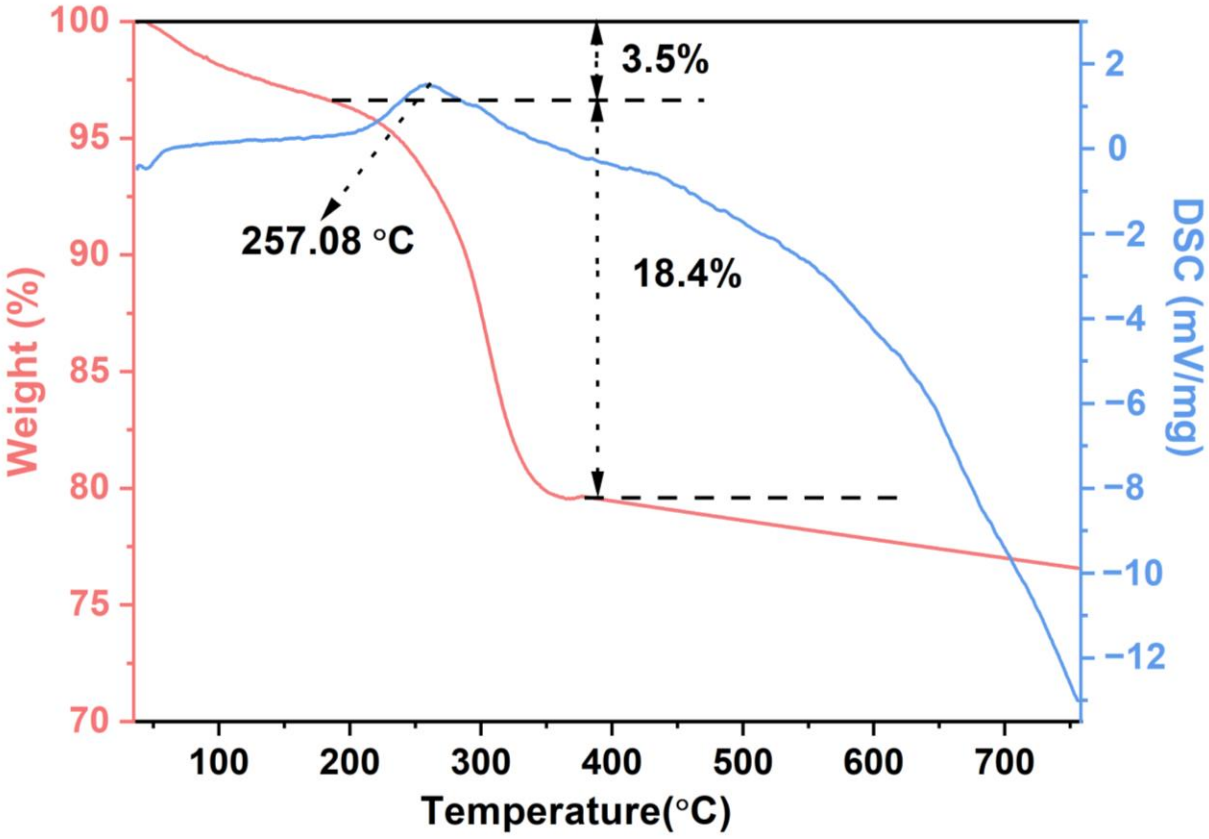

Figure 6. TGA-DSC curve of the formation of $NiFe_2O_4$ precursor.

The gas-sensing performance of $NiFe_2O_4$ is evaluated by the change in the conductance of the sensor in different concentrations of toluene. Figure 8a displays the responses of the sensor based on $NiFe_2O_4$ annealed at 400 °C at a temperature from 180 °C to 260 °C to toluene concentrations of 10 ppm and 30 ppm. Regardless of the toluene concentrations, the sensor shows an increase in its response to the maxmium value at 220 °C and then drops with the further increase in temperature. Due to the insufficient catalytic reaction of the toluene molecules on the $NiFe_2O_4$ surface, the response values are relatively lower at both lower and higher temperatures [55]. Therefore, the following toluene gas-sensing tests were performed at an optimal temperature of 220 °C. Figure 8b shows the dynamic responses of the $NiFe_2O_4$ annealed at 350 °C, 400 °C, and 450 °C to toluene at a concentration of 30 ppm at 220 °C. The S-400 based sensor exhibits a better response of 5.8 compared to the S-350 sensor (2.1) and the S-450 sensor (1.9). Therefore, the gas-sensing performance of the following study is mainly focused on the S-400. As can be seen from Figure 8c, the S-400 sensor shows a good dynamic response to a ppb level of toluene. The $NiFe_2O_4$ sensor (S-400) still shows a response of 1.1 to 50 ppb of toluene, suggesting a low limit of detection (LOD) at the ppb level. Additionally, the dynamic response of the $NiFe_2O_4$ sensor to various toluene concentrations (1–50 ppm) was examined, as shown in Figure 8d. In addition, the relationship between the responses and the toluene concentrations is shown in Figure 8e. We can see that the sensor shows a good dynamic response to toluene at low concentrations from 50 ppb to 5 ppm. A linear relationship between the response (β) and

toluene concentration (C) is fitted by the following equation (Equation (4)), with a relative correlation coefficient of $R^2 = 0.9943$:

$$\beta = 0.5287C + 1.1563 \quad (4)$$

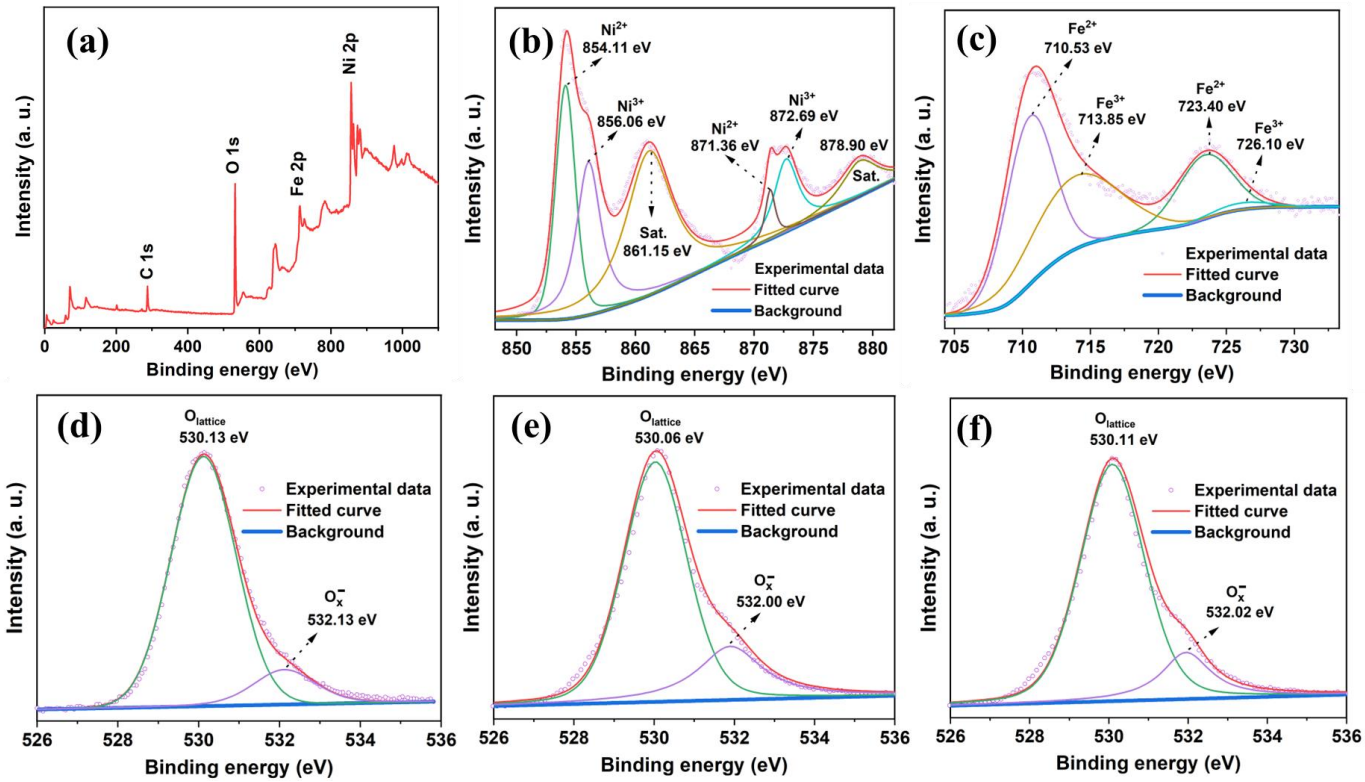

Figure 7. (**a**) The full XPS survey for S-400 $NiFe_2O_4$ and the high-resolution XPS spectra of (**b**) Ni 2p for S-400 $NiFe_2O_4$, (**c**) Fe 2p for S-400 $NiFe_2O_4$, O 1s for (**d**) S-350 $NiFe_2O_4$, (**e**) S-400 $NiFe_2O_4$, and (**f**) S-450 $NiFe_2O_4$.

When the tolenene concentration exceeds 5 ppm, the S-400 $NiFe_2O_4$ sensor gradually becomes saturated. The $NiFe_2O_4$ sensor exhibits a response of 4.7 with a fast response (11.6 s) and recovery (41.9 s) time (Figure 8f) to 10 ppm of toluene. The fast response recovery time is attributed to the loose, porous structure of the ultra-thin nanosheets.

Figure 9a shows the response and recovery time of the $NiFe_2O_4$ gas sensor corresponding to the transient curve in the 0.05–50 ppm concentrations of toluene. The response time of the gas sensor decreases with the increase in toluene concentration. In addition, it shows a longer response time at lower concentrations. Kim et al. proposed a nonlinear reaction–diffusion model to explain the relationship between the response/recovery time and gas concentration [56], as shown in following equation:

$$\tau = k{x_0}^2{C_0}^{r-1}/D \quad (5)$$

where k, x_0, C_0, and D represent the reaction rate constant, film thickness, gas concentration, and diffusion coefficient, respectively. According to Equation (5), the gas sensor exhibits a fast response in a high concentration of toluene due to the rapid diffusion via large kinetics. Due to the slower kinetic process of adsorption–desorption and the ionization of surface oxygen during recovery [57], a longer recovery time is needed for a higher gas concentration. In brief, our $NiFe_2O_4$ sensor shows a comparable sensing performance for toluene detection compared with typical sensing materials in the literature, as summarized in Table 3. On the other hand, the responses toward other tested gases with concentrations of 10 ppm, such as xylene, acetone, ethanol, methanol, isopropanol, n-butyl alcohol, formaldehyde, and

ammonia, have been examined, as shown in Figure 9b. Obviously, the response to toluene is about 2–3 times than that of the interfering gases due to the catalytic feature of p-type $NiFe_2O_4$ to toluene at the optimal operating temperature of 220 °C [58].To investigate the short-term repeatability, five consecutive tests of 10 ppm and 30 ppm of toluene were verified, as shown in Figure 9c, which shows a good repeatability. Finally, the long-term stability of one month was validated in Figure 9d. For instance, the responses to 30 ppm of toluene fluctuate around 6.1, suggesting a good stability over a long period of time. The sensor based on porous, tremella-like $NiFe_2O_4$ with nanosheets has the characteristics of a high response, a low detection limit, and fast response and recovery times, which are conductive to practical applications in toluene detection.

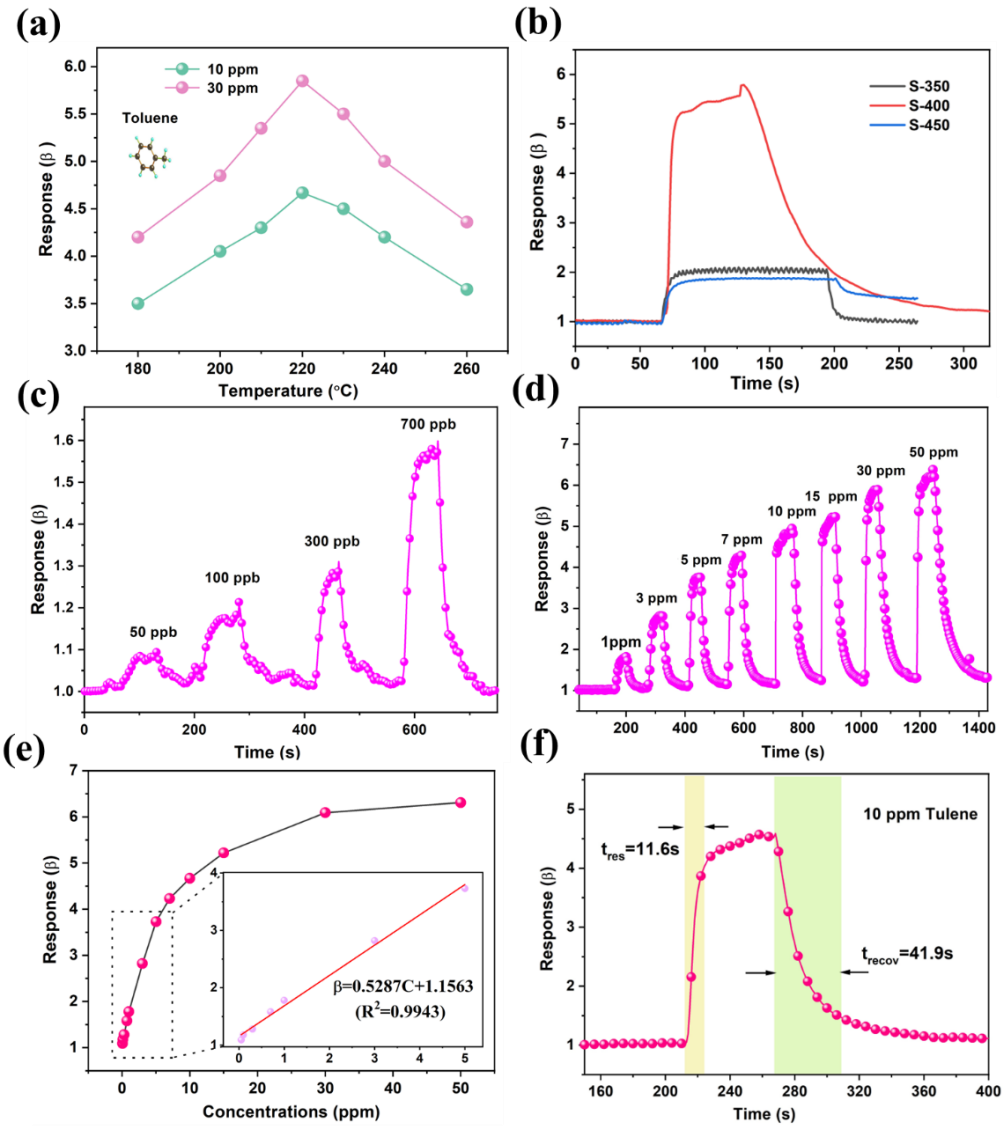

Figure 8. (**a**) Responses of the $NiFe_2O_4$ sensor at different operating temperature to 10 ppm and 30 ppm toluene based on the S-400 $NiFe_2O_4$ sensor; (**b**) responses of the S-350, S-400, and S-450 $NiFe_2O_4$ sensors toward 30 ppm toluene at 220 °C; the dynamic response of the sensor toward (**c**) 50 ppb–700 ppb and (**d**) 1 ppm–50 ppm toluene based on S-400 $NiFe_2O_4$ sensor; (**e**) the relationship between response and toluene concentration (inset is the linear fit) based on S-400 $NiFe_2O_4$ sensor; (**f**) dynamic sensing transient of the $NiFe_2O_4$ to 10 ppm toluene based on S-400 $NiFe_2O_4$ sensor.

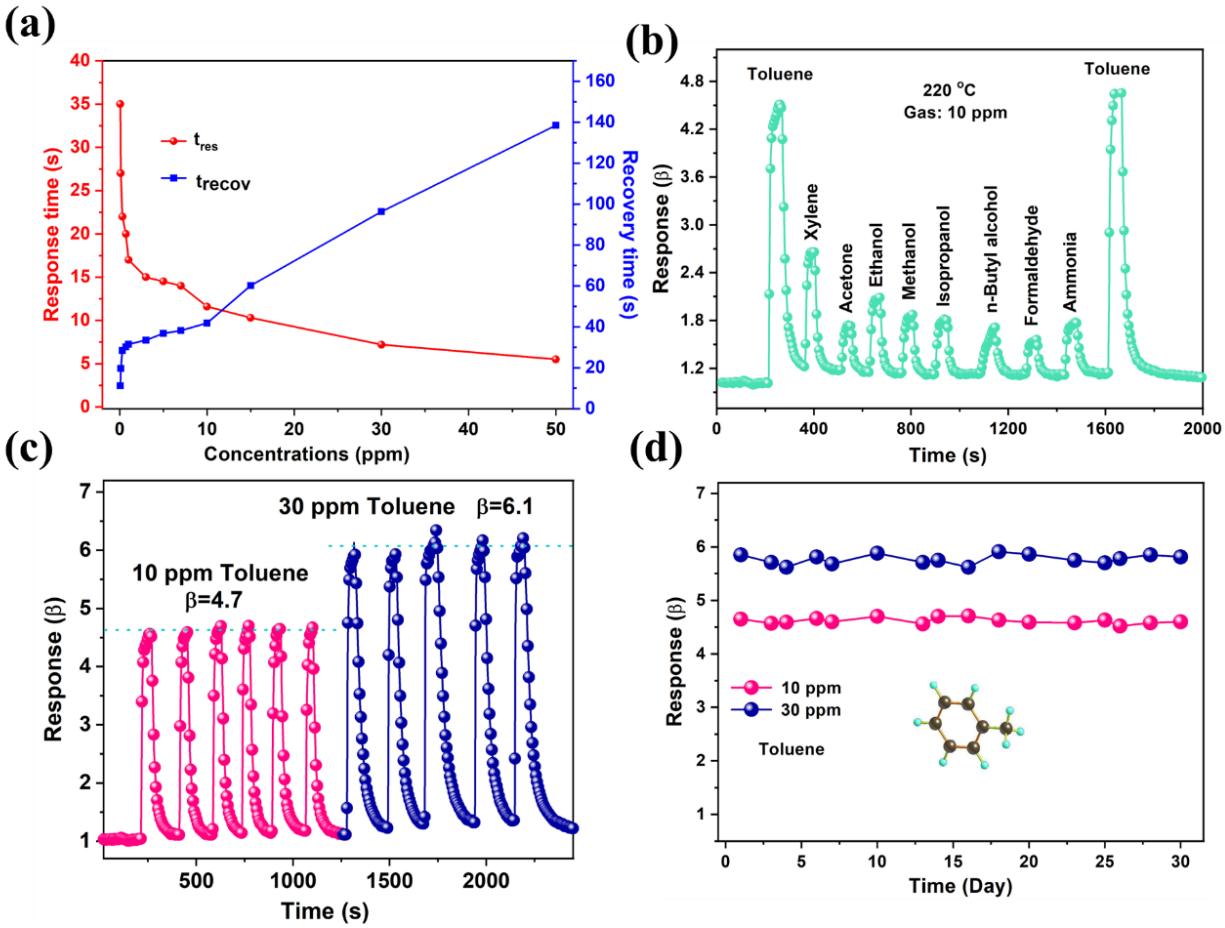

Figure 9. (**a**) The relationship between the response–recovery time and the toluene concentration based on S-400 $NiFe_2O_4$ sensor, (**b**) the selectivity of the sensor to 10 ppm gas at 220 °C based on S-400 $NiFe_2O_4$ sensor, (**c**) the response of the $NiFe_2O_4$ sensor exposed into 10 ppm and 30 ppm toluene at 220 °C based on S-400 $NiFe_2O_4$ sensor, and (**d**) the long-term stability of the sensor to 10 ppm and 30 ppm toluene based on S-400 $NiFe_2O_4$ sensor.

Table 3. Comparision of sensing performances to toluene based on typical sensing materials.

Materials	Microstructures	T (°C)	Response	LOD	τ_{res}/τ_{recov} (s)	Ref.
NiO	Nanopaticle	250	1.5@300 ppm	100 ppm	-	[59]
NiO	Flower-like	250	1.73@0.5 ppm	0.5 ppm	13.6/24.5@2 ppm	[60]
In_2O_3	Nanotube	340	10.9@100 ppm	1 ppm	17/40@40 ppm	[61]
WO_3	Nanopaticle	225	132 @100 ppm	2 ppm	2/6@100 ppm	[62]
TiO_2	Nanopaticle	327	5.15@1 ppm	5 ppb	-	[63]
Zn_2SnO_4	Nanosheet	280	4.7@5 ppm	5 ppm	1/3.55@10 ppm	[64]
SnO_2	Sphere	400	20.2@50 ppm	-	52/74@50 ppm	[65]
$NiFe_2O_4$	Nano-octahedron	260	6.41@100 ppm	1 ppm	25/40@100 ppm	[66]
$NiFe_2O_4$	Tremella-like	220	4.67@10 ppm	50 ppb	11.6/41.9@10 ppm	This work

T: temperature; LOD: limit of detection; Ref.: references.

As a widely accepted sensing mechanism, the adsorbeed oxygen species (O^-, O^{2-} and O_2^-) play an crucial role in determining the sensing performance of a sensor based on semiconductor oxides. The $NiFe_2O_4$ is a p-type semiconductor whose conductivity carriers come from holes. A porous, tremella-like $NiFe_2O_4$ nanosheet reacts with adsorbed oxygen and its toluene target gas as follows [1,67]:

$$O_2(\text{gas}) \rightarrow O_2(\text{adsorbed}) \quad (6)$$

$$O_2(\text{adsorbed}) + e^- \rightarrow O_2^- \quad (7)$$

$$O_2^- + e^- \rightarrow 2O^- \quad (8)$$

$$O^- + e^- \rightarrow O^{2-} \quad (9)$$

$$C_6H_5CH_3 + O^- \rightarrow C_6H_5CHO^- + H_2O \quad (10)$$

$$C_6H_5CH_3 + O^{2-} \rightarrow C_6H_5CHO^- + H_2O + e^- \quad (11)$$

$$C_6H_5CHO^- \rightarrow C_6H_5CHO + e^- \quad (12)$$

When exposed to air, the formation of oxygen species, as confirmed by the above XPS analysis, will capture free electrons from its conductance band. Upon exposure to toluene, the toluene molecules will react with these oxygen species, resulting in the release of the electrons. Accordingly, the change in conductance of the sensor occurs, achieving the detection of toluene. The true resistance change in the $NiFe_2O_4$ sensor at 1 ppm of toluene is shown in Figure 10a. The resistance of around 7.7 kΩ and 13.7 kΩ are tested in the air and in 1 ppm of toluene for the $NiFe_2O_4$ sensor, producing a response of 1.8. Figure 10b shows the reaction of the target gas toluene molecules in the porous nanosheets. First, oxygen is adsorbed onto the surface of the porous nanosheet, which then reacts with electrons in the conduction band, giving rise to active oxygen species (O^-, O^{2-} and $O_2{}^-$). After exposure to the target gas, the toluene molecule will react with active oxygen species to produce benzaldehyde and H_2O molecules, as illustrated by the above equations (Equations (6)–(12)) [60,68].

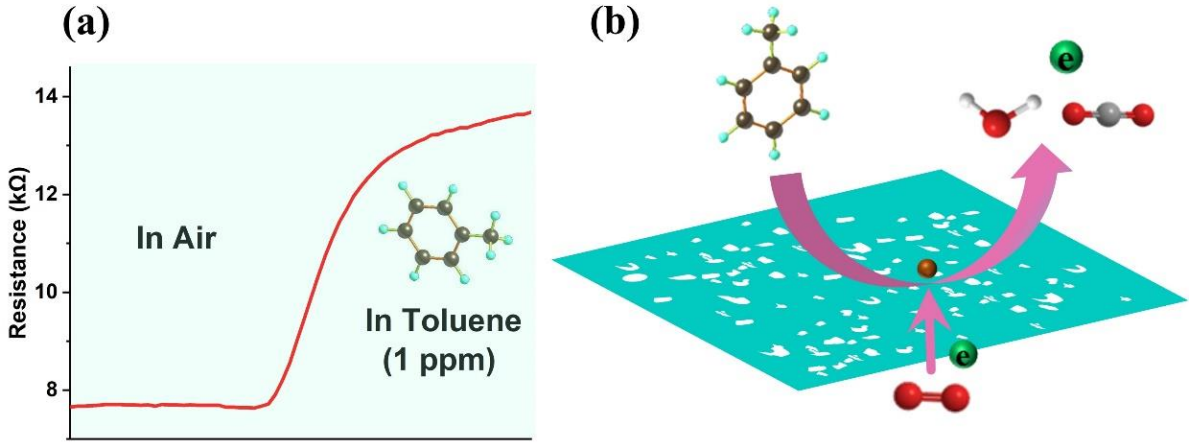

Figure 10. (**a**) The real resitance variation of $NiFe_2O_4$ sensor exposed to air and 1 ppm toluene atmosphere based on S-400 $NiFe_2O_4$ sensor; (**b**) the gas-sensing mechanism based on $NiFe_2O_4$ sensor for toluene detection.

The gas-sensing performance of this sensor is mainly ascribed to the following aspects. Fistly, the gas-sensing performance is derived from the unique spinel structure of the $NiFe_2O_4$, which possesses good catalytic activity. $NiFe_2O_4$ with a spinel structure shows a reversible redox reaction ($Ni^{2+} + h^+ \leftrightarrow Ni^{3+}$, $Fe^{2+} + h^+ \leftrightarrow Fe^{3+}$), resulting in the catalytic ability for the toluene to react on the surface of the $NiFe_2O_4$ at moderate temperatures [69]. Secondly, the unique, tremella-like structure assembled by the ultrathin nanosheets of $NiFe_2O_4$ favors a toluene-gas-sensitive performance. The unique morphology not only possesses a large specific surface area to provide abundant active sites but also provides abundant mesoporous structures as effective channels for gas diffusion. Finally, the porous, ultrathin $NiFe_2O_4$ nanosheet structure plays an important role in the highly sensitive

detection of toluene, especially at low concentrations. The porous nanosheet structure not only provides a large number of active sites for gas reactions but also gas molecule transport channels, offering a preference for the detection of low concentrations of toluene.

4. Conclusions

In summary, the porous, tremella-like $NiFe_2O_4$ assembled with ultrathin nanosheets was successfully synthesized with the assistance of 1,4-phenylenediboronic acid. The band gap of the as-synthesized $NiFe_2O_4$ is around 1.7 eV. The $NiFe_2O_4$ annealed at 400 °C shows better performance at sensing toluene. It exhibits a good response of 4.7, fast response and recovery times of 11.6 s and 41.9 s to 10 ppm of toluene at 220 °C, and a low detection limit of 50 ppb. Our good sensing performance originates from the original catalytic activity of $NiFe_2O_4$, the high surface area (77.80 m^2/g), and the unique porous nanosheet structure. The as-prepared porous, tremella-like $NiFe_2O_4$ with ultrathin nanosheets using 1,4-benzenediboronic acid as a ligand provides a feasible strategy for the fabrication of $NiFe_2O_4$ to detect ppb-level toluene. Finally, it is also worth noting that the response time and selectivity of the $NiFe_2O_4$ sensor toward toluene could be further enhanced by doping, coupling with other sensing materials, or functionalizing noble metal nanoparticles for practical applications.

Author Contributions: Conceptualization, C.D.; Formal analysis, H.Q. and H.G.; Data curation, Y.Z.; Writing—original draft, Y.Z.; Writing—review & editing, C.D. and Z.Y.; Funding acquisition, C.G. and H.G. All authors have read and agreed to the published version of the manuscript.

Funding: This research received no external funding.

Data Availability Statement: The data that support the findings of this study are available within this article.

Acknowledgments: This work was financially supported by the National Natural Science Foundation of China (22165032), the Application Basic Research Fund of Yunnan Province (2019FB129 and 202301AT070207), and the Major Science and Technology Project of Precious Metal Materials Genetic Engineering in Yunnan Province (2019ZE001-6). The authors acknowledge the Advanced Analysis and Measurement Center of Yunnan University for the sample-testing service.

Conflicts of Interest: The authors declare no conflict of interest.

References

1. Mirzaei, A.; Kim, J.-H.; Kim, H.W.; Kim, S.S. Resistive-based gas sensors for detection of benzene, toluene and xylene (BTX) gases: A review. *J. Mater. Chem. C* **2018**, *6*, 4342–4370. [CrossRef]
2. Yücel, M.; Takagi, M.; Walterfang, M.; Lubman, D.I. Toluene misuse and long-term harms: A systematic review of the neuropsychological and neuroimaging literature. *Neurosci. Biobehav. Rev.* **2008**, *32*, 910–926. [CrossRef] [PubMed]
3. Ren, F.; Gao, L.; Yuan, Y.; Zhang, Y.; Alqrni, A.; Al-Dossary, O.M.; Xu, J. Enhanced BTEX gas-sensing performance of CuO/SnO_2 composite. *Sens. Actuators B* **2016**, *223*, 914–920. [CrossRef]
4. Donald, J.M.; Hooper, K.; Hopenhayn-Rich, C. Reproductive and developmental toxicity of toluene: A review. *Environ. Health Perspect.* **1991**, *94*, 237–244.
5. Wheeler, A.J.; Wong, S.L.; Khoury, C.; Zhu, J. Predictors of indoor BTEX concentrations in Canadian residences. *Health Rep.* **2013**, *24*, 11–17.
6. Hermawan, A.; Asakura, Y.; Inada, M.; Yin, S. A facile method for preparation of uniformly decorated-spherical SnO_2 by CuO nanoparticles for highly responsive toluene detection at high temperature. *J. Mater. Sci. Technol.* **2020**, *51*, 119–129. [CrossRef]
7. Zhan, C.; Liu, J.; Cui, M.; Wu, W.; Hao, F.; Wang, Z.; Liu, J.; Zhang, X.; Pan, L.; Deng, M.; et al. Alterations in functional connectivity of executive control network reveal influence of indoor toluene on cognition at low concentration. *Build. Environ.* **2023**, *232*, 110031. [CrossRef]
8. Kim, N.-H.; Choi, S.-J.; Yang, D.-J.; Bae, J.; Park, J.; Kim, I.-D. Highly sensitive and selective hydrogen sulfide and toluene sensors using Pd functionalized WO_3 nanofibers for potential diagnosis of halitosis and lung cancer. *Sens. Actuators B* **2014**, *193*, 574–581. [CrossRef]
9. Seekaew, Y.; Wisitsoraat, A.; Phokharatkul, D.; Wongchoosuk, C.J.S.; Chemical, A.B. Room temperature toluene gas sensor based on TiO_2 nanoparticles decorated 3D graphene-carbon nanotube nanostructures. *Sens. Actuators B* **2019**, *279*, 69–78. [CrossRef]
10. Hunter, G.W.; Akbar, S.A.; Bhansali, S.; Daniele, M.A.; Erb, P.D.; Johnson, K.J.; Liu, C.C.; Miller, D.R.; Oralkan, O.; Hesketh, P.J.; et al. Editors' choice-critical review-a critical review of solid state gas sensors. *J. Electrochem. Soc.* **2020**, *167*, 037570. [CrossRef]

11. Yu, H.; Guo, C.; Zhang, X.; Xu, Y.; Cheng, X.-L.; Gao, S.; Huo, L.-H. Recent development of hierarchical netal oxides based gas sensors: From gas sensing performance to applications. *Adv. Sustain. Syst.* **2022**, *6*, 2100370. [CrossRef]
12. Šutka, A.; Gross, K.A. Spinel ferrite oxide semiconductor gas sensors. *Sens. Actuators B* **2016**, *222*, 95–105. [CrossRef]
13. Olowoyo, J.O.; Kriek, R.J. Recent Progress on Bimetallic-Based Spinels as Electrocatalysts for the Oxygen Evolution Reaction. *Small* **2022**, *18*, 2203125. [CrossRef] [PubMed]
14. Kaneti, Y.V.; Septiani, N.L.W.; Saptiama, I.; Jiang, X.; Yuliarto, B.; Shiddiky, M.J.A.; Fukumitsu, N.; Kang, Y.-M.; Golberg, D.; Yamauchi, Y. Self-Sacrificial Templated Synthesis of a Three-Dimensional Hierarchical Macroporous Honeycomb-like ZnO/$ZnCo_2O_4$ Hybrid for Carbon Monoxide Sensing. *J. Mater. Chem. A* **2019**, *7*, 3415–3425. [CrossRef]
15. Kim, S.-H.; Yun, K.-S. Room-temperature hydrogen gas sensor composed of palladium thin film deposited on $NiCo_2O_4$ nanoneedle forest. *Sens. Actuators B* **2023**, *376*, 132958. [CrossRef]
16. Guan, Y.; Yin, C.; Cheng, X.; Liang, X.; Diao, Q.; Zhang, H.; Lu, G. Sub-ppm H2S sensor based on YSZ and hollow balls $NiMn_2O_4$ sensingelectrode. *Sens. Actuators B* **2014**, *193*, 501–508. [CrossRef]
17. Lai, X.; Cao, K.; Shen, G.; Xue, P.; Wang, D.; Hu, F.; Zhang, J.; Yang, Q.; Wang, X. Ordered mesoporous $NiFe_2O_4$ with ultrathin framework for low-ppb toluene sensing. *Sci. Bull.* **2018**, *63*, 187–193. [CrossRef]
18. Karuppasamy, K.; Sharma, B.; Vikraman, D.; Jo, E.-B.; Sivakumar, P.; Kim, H.-S. Switchable p-n gas response for 3D-hierarchical $NiFe_2O_4$ porous microspheres for highly selective and sensitive toluene gas sensors. *J. Alloys Compd.* **2021**, *886*, 161281. [CrossRef]
19. Yang, L.; Xie, Y.; Zhao, H.; Wu, X.; Wang, Y. Preparation and gas-sensing properties of $NiFe_2O_4$ semiconductor materials. *Solid-State Electron.* **2005**, *49*, 1029–1033. [CrossRef]
20. Zhang, Y.; Jia, C.; Wang, Q.; Kong, Q.; Chen, G.; Guan, H.; Dong, C. Highly sensitive and selective toluene sensor of bimetallic Ni/Fe-MOFs derived porous $NiFe_2O_4$ nanorods. *Ind. Eng. Chem. Res.* **2019**, *58*, 9450–9457. [CrossRef]
21. Cho, K.; Kang, C.W.; Ryu, S.H.; Jang, J.Y.; Son, S.U. The rise of morphology-engineered microporous organic polymers (ME-MOPs): Synthesis and benefits. *J. Mater. Chem. A* **2022**, *10*, 6950–6964. [CrossRef]
22. Hu, M.-L.; Masoomi, M.Y.; Morsali, A. Template strategies with MOFs. *Coord. Chem. Rev.* **2019**, *387*, 415–435. [CrossRef]
23. Wen, T.; Liu, M.; Chen, S.; Li, Q.; Du, Y.; Zhou, T.; Ritchie, C.; Zhang, J.S. 2D boron imidazolate framework nanosheets with electrocatalytic applications for oxygen evolution and carbon dioxide reduction reaction. *Small* **2020**, *16*, 1907669. [CrossRef] [PubMed]
24. Shen, D.; Chen, X.; Luo, J.; Wang, Y.; Sun, Y.; Pan, J. Boronate affinity imprinted Janus nanosheets for macroscopic assemblies: From amphiphilic surfactants to porous sorbents for catechol adsorption. *Sep. Purif. Technol.* **2021**, *256*, 117837. [CrossRef]
25. Zhang, Q.-P.; Sun, N.; Zheng, J.; Wang, S.-W.; Wu, Y.; Luo, D.-L.; Zhou, Y.-L. Fabrication of lead borate single crystal nanosheets for attenuating both neutron and gamma radiations. *Adv. Eng. Mater.* **2017**, *19*, 1600650. [CrossRef]
26. Dimowa, L.; Nikolova, R.; Dyulgerov, V.; Kostov-Kytin, V.; Shivachev, B. Synthesis of MOFs from Zn,Cd,Ni-4-carboxyphenylboronic acid with DMF solvent. *Acta Crystallogr. A* **2014**, *70*, C1129. [CrossRef]
27. Abdallah, A.; Daiguebonne, C.; Suffren, Y.; Rojo, A.; Demange, V.; Bernot, K.; Calvez, G.; Guillou, O. Microcrystalline core-shell lanthanide-based coordination polymers for unprecedented luminescent properties. *Inorg. Chem.* **2019**, *58*, 1317–1329. [CrossRef]
28. Dong, C.; Tian, R.; Zhang, Y.; Liu, K.; Chen, G.; Guan, H.; Yin, Z. MOF-on-MOF nanoarchitecturing of Fe_2O_3@$ZnFe_2O_4$ radial-heterospindles towards multifaceted superiorities for acetone detection. *Chem. Eng. J.* **2022**, *442*, 136094. [CrossRef]
29. Dong, C.; Tian, R.; Qu, H.; Tan, H.; Chen, G.; Guan, H.; Yin, Z. Anchoring Pt particles onto mesoporousized ZnO holey cubes for triethylamine detection with multifaceted superiorities. *Small* **2023**, *19*, 2300756. [CrossRef]
30. Henderson, B.; Imbusch, G.F. *Optical Spectroscopy of Inorganic Solids*; Oxford University Press: New York, NY, USA, 1989.
31. Tien, N.A.; Mittova, V.; Sladkopevtsev, B.; Mai, V.; Mittova, I.; Vuong, B. Structural, optical and magnetic properties of Y-doped $NiFe_2O_4$ nanoparticles prepared by simple co-precipitation method. *Mater. Solid State Sci.* **2023**, *138*, 107149. [CrossRef]
32. Chiad, B.T.; Mohammed, R.A. Spectroscopy, optical properties of $NiFe_2O_4$ nanoparticles prepared by co-sputtering technique in different gasses mixture ratio. *Int. J. New Technol. Res.* **2017**, *3*, 56–58.
33. Tong, S.-K.; Chi, P.-W.; Kung, S.-H.; Wei, D.-H. Tuning bandgap and surface wettability of $NiFe_2O_4$ driven by phase transition. *Sci. Rep.* **2018**, *8*, 1338. [CrossRef] [PubMed]
34. Gupta, N.K.; Ghaffari, Y.; Kim, S.; Bae, J.; Kim, K.S.; Saifuddin, M. Photocatalytic degradation of organic pollutants over MFe_2O_4 (M=Co, Ni, Cu, Zn) nanoparticles at neutral pH. *Sci. Rep.* **2020**, *10*, 4942. [CrossRef]
35. Dileep, K.; Louaya, B.; Pachauri, N.; Gupta, A.; Datta, R. Probing optical band gaps at the nanoscale in $NiFe_2O_4$ and $CoFe_2O_4$ epitaxial films by high resolution electron energy loss spectroscopy. *J. Appl. Phys.* **2014**, *116*, 103505. [CrossRef]
36. Sun, Q.C.; Mazumdar, D.; Ma, J.X.; Holinsworth, B.S.; O'Neal, K.R.; Kim, G.; Butler, W.H.; Gupta, A.; Musfeldt, J.L. Optical band gap hierarchy in a magnetic oxide: Electronic structure of $NiFe_2O_4$. *Phys. Rev. B* **2012**, *86*, 205106. [CrossRef]
37. Timmerman, M.A.; Xia, R.; Le, P.T.P.; Wang, Y.; ten Elshof, J.E. Metal oxide nanosheets as 2D building blocks for the design of novel materials. *Chem. Eur. J.* **2020**, *26*, 9084–9098. [CrossRef] [PubMed]
38. Sing, K.S.W. Reporting physisorption data for gas/solid systems with special reference to the determination of surface area and porosity (Recommendations 1984). *Pure Appl. Chem.* **1985**, *57*, 603–619. [CrossRef]
39. Majhi, S.M.; Ali, A.; Rai, P.; Greish, Y.E.; Alzamly, A.; Surya, S.G.; Qamhieh, N.; Mahmoud, S.T. Metal-organic frameworks for advanced transducer based gas sensors: Review and perspectives. *Nanoscale Adv.* **2022**, *4*, 697–732. [CrossRef]
40. Liu, N.; Wang, X.-F.; Zhang, G.; Liang, H.; Li, T.; Zhao, Y.; Zhang, T.; Tan, Z.; Song, X.-Z. Metal-organic framework-derived porous $NiFe_2O_4$ nanoboxes for ethyl acetate gas sensors. *ACS Appl. Nano Mater.* **2022**, *5*, 14320–14327. [CrossRef]

41. Song, X.-Z.; Meng, Y.-L.; Chen, X.; Sun, K.-M.; Wang, X.-F. Hollow $NiFe_2O_4$ hexagonal biyramids for high-performance n-propanol sensing at low temperature. *New J. Chem.* **2018**, *42*, 14071–14074. [CrossRef]
42. Zhang, Y.; Zhou, Y.; Li, Z.; Chen, G.; Mao, Y.; Guan, H.; Dong, C. MOFs-derived $NiFe_2O_4$ fusiformis with highly selective response to xylene. *J. Alloys Compd.* **2019**, *784*, 102–110. [CrossRef]
43. Zhou, T.; Zhang, T.; Zeng, Y.; Zhang, R.; Lou, Z.; Deng, J.; Wang, L. Structure-driven efficient $NiFe_2O_4$ materials for ultra-fast response electronic sensing platform. *Sens. Actuators B* **2018**, *255*, 1436–1444. [CrossRef]
44. Bameri, I.; Saffari, J.; Baniyaghoob, S.; Ekrami-Kakhki, M.-S. Synthesis of magnetic nano-$NiFe_2O_4$ with the assistance of ultrasound and its application for photocatalytic degradation of Titan Yellow: Kinetic and isotherm studies. *Colloids Interface Sci. Commun.* **2022**, *48*, 100610. [CrossRef]
45. Zeynizadeh, B.; Mohammadzadeh, I.; Shokri, Z.; Ali Hosseini, S. Synthesis and characterization of $NiFe_2O_4$@Cu nanoparticles as a magnetically recoverable catalyst for reduction of nitroarenes to arylamines with $NaBH_4$. *J. Colloid Interface Sci.* **2017**, *500*, 285–293. [CrossRef] [PubMed]
46. Toghan, A.; Khairy, M.; Kamar, E.M.; Mousa, M.A. Effect of particle size and morphological structure on the physical properties of $NiFe_2O_4$ for supercapacitor application. *J. Mater. Res. Technol.* **2022**, *19*, 3521–3535. [CrossRef]
47. Wang, X.-M.; Hu, Z.-J.; Guo, P.-F.; Chen, M.-L.; Wang, J.-H. Boron-modified defect-rich molybdenum disulfide nanosheets: Reducing nonspecific adsorption and promoting a high capacity for isolation of immunoglobulin G. *ACS Appl. Mater. Interfaces* **2020**, *12*, 43273–43280. [CrossRef]
48. Ling, Z.; Wang, Z.; Zhang, M.; Yu, C.; Wang, G.; Dong, Y.; Liu, S.; Wang, Y.; Qiu, J. Sustainable synthesis and assembly of biomass-derived B/N co-doped carbon nanosheets with ultrahigh aspect ratio for high-performance supercapacitors. *Adv. Funct. Mater.* **2016**, *26*, 111–119. [CrossRef]
49. Wei, H.; Zhang, H.; Song, B.; Yuan, K.; Xiao, H.; Cao, Y.; Cao, Q. Metal–Organic Framework (MOF) Derivatives as Promising Chemiresistive Gas Sensing Materials: A Review. *Int. J. Environ. Res. Public Health* **2023**, *20*, 4388. [CrossRef]
50. Yang, H.; Liu, Y.; Luo, S.; Zhao, Z.; Wang, X.; Luo, Y.; Wang, Z.; Jin, J.; Ma, J. Lateral-size-mediated efficient oxygen evolution reaction: Insights into the atomically thin quantum dot structure of $NiFe_2O_4$. *ACS Catal.* **2017**, *7*, 5557–5567. [CrossRef]
51. Wu, Z.; Zou, Z.; Huang, J.; Gao, F. $NiFe_2O_4$ nanoparticles/NiFe layered double-hydroxide nanosheet heterostructure array for efficient overall water splitting at large current densities. *ACS Appl. Mater. Interfaces* **2018**, *10*, 26283–26292. [CrossRef]
52. Jia, Y.; Jian, B.; Wang, X.; Wang, C.; Sun, Y.; Zhang, H.; Shimanoe, K.; Lu, G. MOF-derived porous NiO/$NiFe_2O_4$ nanocubes for improving the acetone detection. *Sens. Actuators B* **2022**, *366*, 131985.
53. Hussain, A.; Zhang, X.; Shi, Y.; Bushira, F.A.; Barkae, T.H.; Ji, K.; Guan, Y.; Chen, W.; Xu, G. Generation of oxygen vacancies in metal-organic framework-derived one-dimensional $Ni_{0.4}Fe_{2.6}O_4$ nanorice heterojunctions for ppb-level diethylamine gas sensing. *Anal.Chem.* **2023**, *95*, 1747–1754. [CrossRef]
54. Shuai, Y.; Peng, R.; He, Y.; Liu, X.; Wang, X.; Guo, W. NiO/$BiVO_4$ p-n heterojunction microspheres for conductometric triethylamine gas sensors. *Sens. Actuators B* **2023**, *384*, 133625. [CrossRef]
55. Wang, C.; Cheng, X.; Zhou, X.; Sun, P.; Hu, X.; Shimanoe, K.; Lu, G.; Yamazoe, N. Hierarchical α-Fe_2O_3/NiO composites with a hollow structure for a gas sensor. *ACS Appl. Mater. Interfaces* **2014**, *6*, 12031–12037. [CrossRef] [PubMed]
56. Choi, S.-J.; Chattopadhyay, S.; Kim, J.J.; Kim, S.-J.; Tuller, H.L.; Rutledge, G.C.; Kim, I.-D. Coaxial electrospinning of WO_3 nanotubes functionalized with bio-inspired Pd catalysts and their superior hydrogen sensing performance. *Nanoscale* **2016**, *8*, 9159–9166. [CrossRef]
57. Wen, Z.; Tian-mo, L. Gas-sensing properties of SnO_2-TiO_2-based sensor for volatile organic compound gas and its sensing mechanism. *Physica B Condens. Matter* **2010**, *405*, 1345–1348. [CrossRef]
58. Song, X.-Z.; Sun, F.-F.; Dai, S.-T.; Lin, X.; Sun, K.-M.; Wang, X.-F. Hollow $NiFe_2O_4$ microspindles derived from Ni/Fe bimetallic MOFs for highly sensitive acetone sensing at low operating temperatures. *Inorg.Chem. Front.* **2018**, *5*, 1107–1114. [CrossRef]
59. Liu, H.; He, Y.; Nagashima, K.; Meng, G.; Dai, T.; Tong, B.; Deng, Z.; Wang, S.; Zhu, N.; Yanagida, T.; et al. Discrimination of VOCs molecules via extracting concealed features from a temperature-modulated p-type NiO sensor. *Sens. Actuators B* **2019**, *293*, 342–349. [CrossRef]
60. Yuan, C.; Li, H.; Xie, L.; Wang, F.; Deng, H.; Chang, F.; Sun, Y. Flower-like NiO nanostructures synthesized by electrodeposition method for efficient detection of toluene gas. *RSC Adv.* **2015**, *5*, 92128–92133. [CrossRef]
61. Chi, X.; Liu, C.; Liu, L.; Li, H.; He, Y.; Bo, X.; Liu, L. Toluene-sensing properties of In_2O_3 nanotubes synthesized by electrospinning. *J. Semicond.* **2014**, *35*, 064005. [CrossRef]
62. Wang, X.; Chen, F.; Yang, M.; Guo, L.; Xie, N.; Kou, X.; Song, Y.; Wang, Q.; Sun, Y. Dispersed WO_3 nanoparticles with porous nanostructure for ultrafast toluene sensing. *Sens. Actuators B* **2019**, *289*, 195–206. [CrossRef]
63. Kang, Y.; Kim, K.; Cho, B.; Kwak, Y.; Kim, J. Highly Sensitive Detection of Benzene, Toluene, and Xylene Based on CoPP-Functionalized TiO_2 Nanoparticles with Low Power Consumption. *ACS Sens.* **2020**, *5*, 754–763. [CrossRef] [PubMed]
64. Wang, L.; Zhou, T.; Zhang, R.; Lou, Z.; Deng, J.; Zhang, T. Comparison of toluene sensing performances of zinc stannate with different morphology-based gas sensors. *Sens. Actuators B* **2016**, *227*, 448–455. [CrossRef]
65. Hermawan, A.; Asakura, Y.; Inada, M.; Yin, S. One-step synthesis of micro-/mesoporous SnO_2 spheres by solvothermal method for toluene gas sensor. *Ceram. Int.* **2019**, *45*, 15435–15444. [CrossRef]
66. Zhang, Y.; Jia, C.; Wang, Q.; Kong, Q.; Chen, G.; Guan, H.; Dong, C. MOFs-derived porous $NiFe_2O_4$ nano-octahedrons with hollow interiors for an excellent toluene gas sensor. *Nanomaterials* **2019**, *9*, 1059. [CrossRef]

67. Kim, H.-J.; Lee, J.-H. Highly sensitive and selective gas sensors using p-type oxidesemiconductors: Overview. *Sens. Actuators B* **2014**, *192*, 607–627. [CrossRef]
68. Lyu, Y.; Li, C.; Du, X.; Zhu, Y.; Zhang, Y.; Li, S. Catalytic oxidation of toluene over MnO_2 catalysts with different Mn (II) precursors and the study of reaction pathway. *Fuel* **2020**, *262*, 116610. [CrossRef]
69. Zhou, T.; Zhang, R.; Wang, Y.; Zhang, T. MOF-derived 1 D α-Fe_2O_3/$NiFe_2O_4$ heterojunction as efficient sensing materials of acetone vapors. *Sens. Actuators B* **2019**, *281*, 885–892. [CrossRef]